



**HAL**  
open science

# Giant impacts, heterogeneous mantle heating and a past hemispheric dynamo on Mars

Julien Monteux, Hagay Amit, Gael Choblet, Benoit Langlais, G. Tobie

## ► To cite this version:

Julien Monteux, Hagay Amit, Gael Choblet, Benoit Langlais, G. Tobie. Giant impacts, heterogeneous mantle heating and a past hemispheric dynamo on Mars. *Physics of the Earth and Planetary Interiors*, 2015, 240, pp.114-124. <10.1016/j.pepi.2014.12.005>. <hal-01142028>

**HAL Id: hal-01142028**

**<https://hal.science/hal-01142028v1>**

Submitted on 16 Jan 2018

**HAL** is a multi-disciplinary open access archive for the deposit and dissemination of scientific research documents, whether they are published or not. The documents may come from teaching and research institutions in France or abroad, or from public or private research centers.

L'archive ouverte pluridisciplinaire **HAL**, est destinée au dépôt et à la diffusion de documents scientifiques de niveau recherche, publiés ou non, émanant des établissements d'enseignement et de recherche français ou étrangers, des laboratoires publics ou privés.



HAL Authorization

# Giant impacts, heterogeneous mantle heating and a past hemispheric dynamo on Mars

Julien Monteux<sup>a,b,c\*</sup>, Hagay Amit<sup>a</sup>, Gaël Choblet<sup>a</sup>, Benoit Langlais<sup>a</sup>, Gabriel Tobie<sup>a</sup>

November 12, 2014

<sup>a</sup> *Laboratoire de Planétologie et Géodynamique, Université de Nantes, CNRS, UMR-6112, 2 rue de la Houssinière, 44322 Nantes Cedex, France*

<sup>b</sup> *ISTerre, Université de Grenoble 1, CNRS, Grenoble, France*

<sup>c</sup> *Laboratoire Magmas et Volcans, Université Blaise Pascal - CNRS - IRD, OPGC, 5 rue Kessler, 63038 Clermont Ferrand*

\* Corresponding author.

*E-mail address:* j.monteux@opgc.univ-bpclermont.fr (J. Monteux).

## Abstract

The martian surface exhibits a strong dichotomy in elevation, crustal thickness and magnetization between the southern and northern hemispheres. A giant impact has been proposed as an explanation for the formation of the Northern Lowlands on Mars. Such an impact probably led to strong and deep mantle heating which may have had implications on the magnetic evolution of the planet. We model the effects of such an impact on the martian magnetic field by imposing an impact induced thermal heterogeneity, and the subsequent heat flux heterogeneity, on the martian core-mantle boundary (CMB). The CMB heat flux lateral variations as well as the reduction in the mean CMB heat flux are determined by the size and geographic location of the impactor. A polar impactor leads to a north-south hemispheric magnetic dichotomy that is stronger than an east-west dichotomy created by an equatorial impactor. The amplitude of the hemispheric magnetic dichotomy is mostly controlled by the horizontal Rayleigh number  $Ra_h$  which represents the vigor of the convection driven by the lateral variations of the CMB heat flux. We show that, for a given  $Ra_h$ , an impact induced CMB heat flux heterogeneity is more efficient

28 than a synthetic degree-1 CMB heat flux heterogeneity in generating strong hemispheric  
29 magnetic dichotomies. Large  $Ra_h$  values are needed to get a dichotomy as strong as the  
30 observed one, favoring a reversing paleo-dynamo for Mars. Our results imply that an  
31 impactor radius of  $\sim 1000$  km could have recorded the magnetic dichotomy observed in  
32 the martian crustal field only if very rapid post-impact magma cooling took place.

33 Keywords: Mars, dynamo, magnetic field, core-mantle boundary, impact, heat flux.

## 34 **1 Introduction**

35 Giant impacts have strongly influenced the internal structure and dynamics of the terrestrial  
36 planets during the primordial stages of their evolutions (Hartmann and Davis, 1975; Benz  
37 et al., 1988; Asphaug et al., 2006; Andrews-Hanna et al., 2008; Marinova et al., 2008; Nimmo  
38 et al., 2008; Jutzi and Asphaug, 2011). These events are plausible explanations for remarkable  
39 features of the solar system such as the small volume of Mercury’s mantle relative to its core  
40 (Benz et al., 1988; Gladman and Coffey, 2009), the Earth-Moon system (Canup, 2004) and the  
41 topographic martian and lunar hemispheric dichotomies (Marinova et al., 2008; Nimmo et al.,  
42 2008; Jutzi and Asphaug, 2011). Giant impacts have also been invoked to explain the initiation  
43 or cessation of the dynamos of the terrestrial planets and moons (Roberts et al., 2009; Arkani-  
44 Hamed and Olson, 2010; Reese and Solomatov, 2010; Monteux et al., 2013; Monteux and  
45 Arkani-Hamed, 2014). In these models, the impactors’ radii typically range between 100 and  
46 1000 km. These impacts deliver a large amount of heat to the deep mantle, which is likely to  
47 strongly affect the efficiency of core cooling and in turn the dynamo activity. Although there  
48 is a higher probability that a giant impact will fall on low-latitudes of the planetary surface  
49 (Le Feuvre and Wieczorek, 2011), true polar wander events can ultimately place the resulting  
50 thermal anomaly at high-latitudes of the CMB. Moreover, large impacts could be responsible  
51 for significant resurfacing and reset the magnetization of the pre-impact material (Langlais and  
52 Thébault, 2011; Lillis et al., 2013).

53 On Earth, the influence of lower mantle thermal heterogeneity on core magnetohydro-  
54 dynamics has been extensively studied using numerical dynamos with imposed non-uniform  
55 outer boundary conditions. It has been shown that heterogeneous core-mantle boundary (CMB)  
56 heat flux causes a deviation from axisymmetry in the core flow (Aubert et al., 2007), in the

57 time-average paleomagnetic field (Olson and Christensen, 2002) and in locations of intense  
58 magnetic flux patches on millennial time-scales (Bloxham, 2002; Amit et al., 2010). It may  
59 also explain the emergence of intense magnetic flux patches in the equatorial region (Amit and  
60 Choblet, 2012) and may even yield field locking (Gubbins et al., 2007; Willis et al., 2007). Het-  
61 erogeneous CMB heat flux may also recover the lateral variations in the inner-core boundary  
62 seismic properties (Aubert et al., 2008; Amit and Choblet, 2009). Finally, reversal frequency  
63 and the trajectory of the paleomagnetic dipole axis during reversals may also be governed  
64 by the heterogeneous lower mantle (Glatzmaier et al., 1999; Kutzner and Christensen, 2004;  
65 Olson et al., 2010, 2013; Olson and Amit, 2014).

66 Heterogeneous mantle control has also been proposed to explain some features of planetary  
67 magnetic fields. Cao et al. (2014) found that high equatorial CMB heat flux breaks the core  
68 flow symmetry and produces north-south asymmetric magnetic fields which may explain the  
69 observed field of Mercury (Anderson et al., 2012). Stanley (2010) argued that temperature  
70 differences in the surrounding envelope of the convective zone of Saturn axisymmetrize its  
71 magnetic field. It has also been proposed that CMB heterogeneity may have controlled the  
72 shape of the current Martian magnetic field (Stanley et al., 2008). Mars is characterized by a  
73 striking magnetic field dichotomy, which is correlated with the topographic dichotomy. The  
74 northern lowlands are mostly devoid of significant magnetic fields. In contrast the southern  
75 highlands exhibit large and in some places intense magnetic field anomalies, up to 1500 nT at  
76 90 km altitude as measured by Mars Global Surveyor (Acuña et al., 1998). This is two orders  
77 of magnitude larger than the crustal magnetic field on Earth. In terms of magnetized material,  
78 this suggests a thick (40 km) and intensely magnetized (up to 12 A/m) lithosphere to produce  
79 the observed magnetic field (Langlais et al., 2004), or any combination of a thinner lithosphere  
80 and a more intense magnetization (e.g. Parker, 2003).

81 The martian magnetic dichotomy can be explained using two end-members scenarios. In  
82 the external scenario, the dynamo was equally strong in both hemispheres, and the resulting  
83 magnetization was equally strong in both hemispheres. Then the magnetization of the northern  
84 hemisphere was removed or erased after the dynamo cessation, e.g., by a giant impact (Nimmo  
85 et al., 2008) or volcanic activity (Lillis et al., 2008). Alternatively a significant magnetization  
86 was never recorded in the northern hemisphere because surface conditions, lithological or

87 alteration processes were different from those in the southern hemisphere (Rochette, 2006;  
88 Quesnel et al., 2009; Chassefière et al., 2013). In the internal scenario, the magnetization is  
89 strong only in the southern hemisphere because the dynamo was hemispheric to begin with  
90 (Langlais and Amit, 2008; Stanley et al., 2008; Amit et al., 2011).

91 Such an hemispheric dynamo could have been driven by CMB heat flux heterogeneity  
92 possibly caused by a very large-scale mantle convection pattern (Harder and Christensen, 1996;  
93 Zhong and Zuber, 2001; Elkins-Tanton et al., 2003, 2005; Ke and Solomatov, 2006; Roberts  
94 and Zhong, 2006) or by a giant impact (Roberts et al., 2009). In this study we propose a  
95 model for the magnetic field dichotomy in which the dynamo hemisphericity (internal origin)  
96 is related to a large impact (external origin) (Stanley et al., 2008; Amit et al., 2011; Dietrich and  
97 Wicht, 2013). For that purpose, we model heterogeneous CMB heat flux resulting from giant  
98 impact heating and investigate its influence on the core dynamo by imposing it as a static,  
99 laterally-varying outer boundary condition on numerical dynamo models. In this approach,  
100 the CMB heat flux pattern and amplitude, as well as the reduction in the mean heat flux with  
101 respect to a reference pre-impact value, are determined by the impactor size, using a synthetic  
102 description of the impact heating zone. In section 2 we describe our method. The results are  
103 presented in section 3. Discussion, post-impact time evolution and applicability of our results  
104 to Mars are given in section 4. Conclusions and possible planetary applications are highlighted  
105 in section 5.

## 106 **2 Method**

### 107 **2.1 Impact heating at the CMB**

108 Large impacts brought to Mars a formidable amount of energy that is a function of the impactor  
109 mass and velocity, the latter strongly depending on the impacted planet radius  $R$ . After a large  
110 collision on a Mars-size body, a significant fraction of this energy is deeply buried as heat  
111 within the mantle and leads to a local temperature increase  $\Delta T_0$  below the impact site. The  
112 size and the shape of the post-impact thermal anomaly depend on several parameters such  
113 as the size of the impactor, the impact velocity and angle, and the structure of the martian

114 mantle. Increasing the size of the impactor leads to an increase of the heated volume while  
115 increasing the impact angle from 0 (head-on impact) to larger values (oblique impacts) reduces  
116 the maximal depth reached by the post-impact thermal anomaly (Pierazzo et al., 1997; Pierazzo  
117 and Melosh, 2000). Here for simplicity, we consider that the volume of the thermal anomaly  
118 only scales with the size of the impactor and we consider the case of a head-on impact. Hence,  
119 the post-impact thermal anomaly in our models is approximately uniform within a spherical  
120 volume (termed isobaric core) with radius  $R_{ic}$  that is 1 to 1.44 times larger than the radius of  
121 the impactor  $R_{imp}$  (Pierazzo et al., 1997; Senshu et al., 2002; Monteux et al., 2013).

122 On Mars, the impactor size invoked to explain the topographic dichotomy ranges between  
123 320 and 1350 km (Marinova et al., 2008; Nimmo et al., 2008). This has to be compared to the  
124 size of the martian mantle. Based on solar tidal deformations, the martian core radius has been  
125 estimated between 1520 and 1840 km (Yoder et al., 2003). For simplicity, we assume a core  
126 radius of 1700 km, which implies a mantle thickness of about 1700 km. Hence, considering  
127 that  $R_{ic} = 1.44R_{imp}$ , the post-impact spherical thermal anomaly is likely to overlap the CMB  
128 for  $R_{imp} > 500$  km. For an impactor radius of  $R_{imp} = 1200$  km, the disruption of the impacted  
129 planet will only occur when the impact velocity reaches values of  $\sim 100$  km/s which is much  
130 larger than the impact velocity  $v_{imp}$  considered here ( $v_{imp} = 5$  km/s) (Tonks and Melosh,  
131 1992; Reese et al., 2010). In our models, we consider that the impactor radius ranges between  
132 600 and 1000 km bearing in mind that larger impactors with larger impact angles could have  
133 similar thermal consequences at the CMB (Pierazzo et al., 1997; Pierazzo and Melosh, 2000).

134 As the volume of the isobaric core is governed by the size of the impactor, the magnitude  
135 of the temperature increase can be directly related to the impact velocity. Making the conser-  
136 vative hypothesis that the impact velocity is close to the martian escape velocity and that the  
137 volume of the isothermal sphere is 3 times larger than the impactor (Senshu et al., 2002; Mon-  
138 teux et al., 2013), the energy balance accounting for heating and melting of both the impactor  
139 and impacted material may lead to a uniform spherical temperature increase of  $\sim 400$  K in the  
140 martian mantle (Monteux et al., 2013). Away from the isothermal sphere, the temperature de-  
141 creases rapidly with distance  $r$  as  $(R_{ic}/r)^m$  with  $m$  typically ranging between 4 and 5 (Senshu  
142 et al., 2002; Monteux et al., 2007).

143

144 Geochemical evidence and crater densities indicate that the martian topographic dichotomy  
145 could have formed within the first 50 Myr of Solar System formation and that the martian  
146 northern hemisphere has been low and stable for nearly all of Mars' history (Zuber, 2001;  
147 Frey et al., 2002; Solomon et al., 2005; Marinova et al., 2008). Hence, the impact-driven tem-  
148 perature increase is superimposed to the pre-impact thermal state of the martian mantle that  
149 strongly depends on the short-lived radiogenic heating, the accretion processes and the dissi-  
150 pation of gravitational energy during the core formation (Senshu et al., 2002; Golabek et al.,  
151 2009; Šrámek et al., 2010). The uncertainties on the relative importance of these processes as  
152 well as the diversity of the processes involved in the core formation lead to a wide range of  
153 plausible early thermal states after the full differentiation of Mars. For simplicity, we assume  
154 here a 1D radially dependent pre-impact mantle temperature field. The choice of this specific  
155 temperature field is not crucial as long as the impact heating of the mantle is predominant. As  
156 shown later, the main parameter affecting the dynamo is the amplitude of the heat-flux hetero-  
157 geneity at the CMB. Before the impact heating, we consider a simplified temperature profile  
158 as in Monteux et al. (2013) with a CMB temperature of  $T = 2000$  K and a convective mantle  
159 temperature of  $\sim 1600$  K (Roberts and Arkani-Hamed, 2012). It should be noted that in reality,  
160 the pre-impact thermal state of the martian mantle was probably much more complicated than  
161 the one used in our models, with lateral heterogeneities as well as radial variations (including  
162 thermal boundary layers and pressure dependence). For simplicity, we do not consider the  
163 changes of mantle properties with depth such as the pressure increase and the corresponding  
164 adiabatic heating. Because we consider here that the mantle temperature above the CMB is  
165 uniform and equal to 1600 K while the core temperature is 2000 K, adding more complex-  
166 ity should slightly decrease the amplitude of the heat flux heterogeneity. However, since the  
167 early martian thermal state is poorly constrained, our simple model may be considered as a  
168 reasonable first step to understand the influence of giant impacts on planetary dynamos.

169 The superposition of the large impact-driven temperature increase leads to a significant  
170 perturbation of the pre-impact homogeneous CMB mean heat flux  $q_0^h$ . To obtain the post-  
171 impact heat flux at the martian CMB for a given impactor radius, we used an impact heating  
172 model similar to the one described in Monteux et al. (2013). A uniform spherical temperature  
173 anomaly rapidly decreasing with distance is superimposed on the martian pre-impact temper-

174 ature field. The impact heating is followed by a thermal re-adjustment within a characteristic  
 175 time that is governed by the rheology of the mantle surrounding the impact-induced thermal  
 176 anomaly. This characteristic time is  $\tau_{imp} \sim 10$  Myr (Monteux et al., 2007). The characteristic  
 177 magnetic diffusion time is  $\tau_\lambda = r_o^2/\lambda$  where  $r_o$  is the core radius and  $\lambda$  is the magnetic diffu-  
 178 sivity (e.g. Bloxham and Jackson, 1991). For Mars  $r_o = 1700$  km and combined with updated  
 179 estimates of the electrical conductivity of molten iron in Earth’s core conditions of  $\lambda \sim 0.5$   
 180  $\text{m}^2/\text{s}$  (Pozzo et al., 2012), these estimates give  $\tau_\lambda \sim 180$  kyr. Since  $\tau_{imp} \gg \tau_\lambda$ , the post  
 181 impact mantle temperature field may be considered constant in our numerical dynamo models.

182 The shock wave also leads to a temperature increase within the core of the impacted planet,  
 183 much stronger in the region directly beneath the impact site. The low-viscosity rotating liquid  
 184 core cannot sustain lateral variations of temperature and the core overturns, resulting in a stably  
 185 stratified temperature which increases with radius. In the case of a homogeneous CMB heat  
 186 flux, the thermal stratification occurs within a few kyr (Arkani-Hamed and Olson, 2010). This  
 187 stratification kills the possible pre-existing core convection, and hence the core dynamo. Then  
 188 it can take up to several tens of Myr to remove this stratification by conductive core heat loss  
 189 (Arkani-Hamed and Olson, 2010). However, a significant fraction of the mantle right above  
 190 the CMB may have experienced melting which facilitated the core cooling. The time needed  
 191 to remove the core excess heat by convection is  $10^3 - 10^4$  yr when considering a molten layer  
 192 above the CMB (Monteux et al., 2011). It is therefore likely that after the impact the martian  
 193 dynamo died during the time needed to generate and remove the post-impact core stratification  
 194 (i.e.  $\sim 10^3 - 10^4$  yr). Then, the dynamo probably re-started, while the impact-driven lower  
 195 mantle anomaly was still in place (during  $\tau_{imp} \sim 10$  Myr). For simplicity, we do not consider  
 196 here the core impact heating and the subsequent rapid thermal readjustment. Our dynamo  
 197 models are convectively unstable throughout the shell, corresponding to the state of the system  
 198 after core stratification has been removed and while the CMB heterogeneity was still in place.  
 199 We discuss this aspect in the conclusion section.

200 As the post-impact mantle temperature reaches the temperature of the core, the heat flux  
 201  $q$  is nearly zero where the isobaric core overlaps with the CMB. Away from the isobaric core  
 202 and along the CMB, the heat flux increases rapidly to its pre-impact mean value  $q_0^h$  (Fig. 1).  
 203 The reduction in the mean CMB heat flux due to the impact corresponds to the relative CMB

204 surface that is heated by the impactor and is defined by  $q_0^r$  as

$$q_0^r = \frac{q_0^h - q_0}{q_0^h} \quad (1)$$

205 where  $q_0$  is the post-impact mean heat flux. The amplitude of the heat flux heterogeneity is  
 206 commonly given by  $q^*$  (Olson and Christensen, 2002) with

$$q^* = \frac{q_{max} - q_{min}}{2q_0} \quad (2)$$

207 where  $q_{max}$  and  $q_{min}$  are the maximal and minimal values of the post-impact heat flux respec-  
 208 tively. In Fig. 1, we show  $q_0^r$  and  $q^*$  obtained from our post-impact heating model as a function  
 209 of the impactor size. As the impactor size increases, the extension of the isobaric core on the  
 210 CMB increases, i.e.  $q_0$  decreases and therefore  $q_0^r$  and  $q^*$  increase. An impactor with a radius  
 211 smaller than  $R_{imp} \sim 500$  km has a negligible effect on the heated surface of the CMB. For  
 212 small impactors a small portion of the CMB is heated so  $q_0 \simeq q_0^h$ , and since  $q_{max} = q_0^h$  and  
 213  $q_{min} = 0$  always hold, for small impactors  $q^* \simeq 0.5$ . An impactor radius of  $R_{imp} \sim 1000$  km  
 214 decreases the mean CMB heat flux by 26.5% and produces an heterogeneity with amplitude  
 215  $q^* \sim 0.67$ . In our models, we limit the impactor radius to 1000 km and consider a head-on  
 216 impact which may represent cases with larger impactors and smaller impact angles (Pierazzo  
 217 et al., 1997; Pierazzo and Melosh, 2000).

218

219 Next we expand the impact-driven CMB heat flux pattern in terms of spherical harmonic  
 220 coefficients (Fig. 2). In order to use it as an outer boundary condition for heat flux in our  
 221 dynamo models, we performed a spherical harmonic expansion truncated at  $\ell_{max} = 20$  (see  
 222 Fig. 2 for  $R_{imp} = 800$  km). First we fit the CMB heat flux with the following analytical  
 223 expression in terms of the angular distance  $\omega$  from the impactor's center:

$$q_\omega = \exp \left[ -\frac{1}{n} \left( \frac{\omega}{\omega_0} \right)^n \right] \quad (3)$$

224 The Gauss-like function (3) avoids undesirable Gibbs effects associated with discontinuous  
 225 gradients on the edge of the imprint of the isobaric core on the CMB. The best fit parameters  
 226 found for the three impactor radii are  $\omega_0 = 15^\circ$  and  $n = 3$  for  $R_{imp} = 600$  km,  $\omega_0 = 30^\circ$  and  
 227  $n = 7$  for  $R_{imp} = 800$  km and  $\omega_0 = 48^\circ$  and  $n = 7$  for  $R_{imp} = 1000$  km.

## 2.2 Numerical dynamo models

We solve the set of self-consistent non-dimensional Boussinesq magnetohydrodynamics equations for dynamo action due to thermal convection of an electrically conducting fluid in a rotating spherical shell (for governing equations and more details see Amit et al., 2011). We use the code MAGIC by Johannes Wicht (Wicht, 2002). We analyze numerical dynamos with rigid insulating boundary conditions. The models differ in the imposed outer boundary heat flux pattern and the amplitude of its variation. A summary of model parameters, outer boundary heat flux patterns, geometries and main results is given in Table 1.

It is likely that Mars has no solid inner core up to the present day (e.g. Schubert and Spohn, 1990; Breuer et al., 2010) and, as a consequence, convection in the early martian dynamo was purely thermal (Amit et al., 2011; Dietrich and Wicht, 2013), driven by secular cooling and perhaps by radioactive heating. This convection mode is highly sensitive to CMB heat flux heterogeneity and may thus break internal dynamo symmetries with relatively moderate heterogeneity amplitudes (Hori et al., 2014). Due to numerical singularity at the center of the planet, we retain in our dynamo models a small inner core with a radius  $r_i/r_o = 0.2$  of the outer core radius. We impose zero heat flux on the inner boundary so that the inner core is convectively passive. Overall, results by Aubert et al. (2009) and Hori et al. (2010) suggest that such a relatively small and passive inner core has little effect on the dynamo models.

Four internal non-dimensional parameters control the dynamo action. The heat flux Rayleigh number (Olson and Christensen, 2002) represents the strength of buoyancy force driving the convection relative to retarding forces

$$Ra = \frac{\alpha g_0 q_0 D^4}{k \kappa \nu} \quad (4)$$

where  $\alpha$  is thermal expansivity,  $g_0$  is gravitational acceleration on the outer boundary at radius  $r_o$ ,  $q_0$  is the mean heat flux across the outer boundary,  $D$  is shell thickness,  $k$  is thermal conductivity,  $\kappa$  is thermal diffusivity and  $\nu$  is kinematic viscosity. The Ekman number represents the ratio of viscous and Coriolis forces

$$E = \frac{\nu}{\Omega D^2} \quad (5)$$

253 The Prandtl number is the ratio of kinematic viscosity to thermal diffusivity

$$Pr = \frac{\nu}{\kappa} \quad (6)$$

254 and the magnetic Prandtl number is the ratio of kinematic viscosity to magnetic diffusivity  $\lambda$

$$Pm = \frac{\nu}{\lambda} \quad (7)$$

255 A fifth non-dimensional number is the amplitude of the outer boundary heat flux heterogeneity  
256 which is expressed by  $q^*$  (see Eq. 2).

257 In all cases a volumetric homogeneous heat source  $\epsilon$  compensates for the loss of heat  
258 through the outer boundary according to

$$-4\pi r_o^2 Pr \left[ \frac{\partial T}{\partial r}(r_o) \right] = \frac{4}{3} \pi (r_o^3 - r_i^3) \epsilon \quad (8)$$

259 where [...] denotes averaging over the outer boundary surface  $S$ . In terms of the non-dimensional  
260 variables  $\left[ \frac{\partial T}{\partial r}(r_o) \right] = 1$ , so for  $r_i/r_o = 0.2$  (the geometry used in the study) the source term is  
261  $\epsilon \simeq 2.42$ . We use moderate amplitudes of CMB heat flux heterogeneity to avoid violation of  
262 the Boussinesq approximation on which the dynamo code relies.

263 Most dynamo models fall into two categories. In the first, the radial field on the CMB is  
264 dominated by an axial dipole component, but the field does not reverse. In the second, the field  
265 is multipolar and dipole reversals occur (Kutzner and Christensen, 2002). Earth-like models  
266 that are both dipole-dominated and reversing are only found in a narrow transitional regime of  
267 parameters space (Olson, 2007; Wicht et al., 2009). Following Amit et al. (2011), we consider  
268 cases from both regimes.

### 269 **2.3 Hemispheric magnetic dichotomy monitoring**

270 The kinetic energy of the impactor is dissipated as a result of the irreversible work done by  
271 shock waves in damaging crustal rocks as well as heating and melting the target material (Pier-  
272 azzo et al., 1997; Senshu et al., 2002; Reese and Solomatov, 2006; Monteux et al., 2011). After  
273 the excavation process, a significant fraction of the material molten by impact is redistributed  
274 heterogeneously at the surface of the impacted planet (Marinova et al., 2008, 2011). The distri-  
275 bution of the molten material is governed by the impact parameters such as the impact velocity

276 and angle. At low impact velocities (6 – 10 km/s) and oblique impact angles (30 – 60°),  
277 50 – 70% of the impact-induced melt distribution might be contained within the area of impact  
278 and 25 – 30% might be deposited at the antipode of the impact site (Marinova et al., 2008).  
279 The impact-induced molten material might be redistributed over a thickness that ranges be-  
280 tween 30 and 50 km (Marinova et al., 2008, 2011). The cooling and the crystallization of the  
281 molten material leads to the formation of the impact induced crust potentially recording the  
282 anomalous dynamo.

283 We consider two end member crust formation scenarios (Amit et al., 2011; Langlais and  
284 Thébault, 2011) as illustrated in Fig. 3. In the case of continuous and homogeneous crust  
285 formation, each part of the martian crust is formed by a large number of incremental and su-  
286 perposed additions (e.g. lava flows, sills, dykes) over an extended period of time. Each new  
287 layer records the magnetic field at its time of cooling below the Curie Temperature, and the  
288 present crustal field at a specific location results from the vertical superposition of the mag-  
289 netization vectors of the various layers (Fig. 3, bottom line). If this crust formation scenario  
290 occurs while the dynamo reverses (Fig. 3, bottom right), the present local crustal field would  
291 thus represent the intensity of a long-term time-average martian paleomagnetic field. In the  
292 extreme case of periodic inversions and layers with equal thicknesses, the superposed opposite  
293 sign magnetization vectors could eventually cancel each other. The other end-member model  
294 assumes a random crust formation where crustal units are formed in relatively rapid events  
295 (Fig. 3, top line). Individual crustal blocks are created randomly both in space and time and  
296 each block acquires a magnetization which only depends on the dynamo field at the time of  
297 cooling. The present local field in this scenario thus results from adjacent magnetization vec-  
298 tors, or in a probabilistic way, from the time-average of the paleofield intensity. It is likely  
299 that neither one of these end-member scenarios represent what actually occurred on Mars, and  
300 rather that the actual way in which the magnetized part of the martian crust formed may be  
301 intermediate between the two scenarios.

302 We follow the statistical measures proposed by Amit et al. (2011) corresponding to these  
303 two end-member crust formation scenarios. In the context of a continuous homogeneous crust  
304 formation scenario, we calculate the ratio of intensities of the time-average field at the planet  
305 surface

$$SN_{cnt} = [|\langle \vec{B} \rangle|]_{sh} / [|\langle \vec{B} \rangle|]_{nh} \quad (9)$$

306 where  $SN$  denotes the ratio between the rms surface average in the southern and northern  
 307 hemispheres and the subscript 'cnt' denotes *continuous* crust formation. In the context of a  
 308 random crust formation scenario, we calculate the magnetic dichotomies based on the time-  
 309 average of the magnetic field intensity

$$SN_{rnd} = [\langle |\vec{B}| \rangle]_{sh} / [\langle |\vec{B}| \rangle]_{nh} \quad (10)$$

310 where the subscript 'rnd' denotes *random*. Eqs. (9)-(10) are applied for the east-west di-  
 311 chotomies  $EW_{cnt}$  and  $EW_{rnd}$  by replacing the summations with the appropriate hemispheres.

312 The relevance of the continuous or random crust formation scenario depends on the rela-  
 313 tion between the cooling time of the Impact Induced Molten Material (IIMM) and the typical  
 314 magnetic timescales. The cooling time of the IIMM strongly depends on the presence of an  
 315 atmosphere that may prevent the IIMM from rapid cooling (e.g. Lebrun et al., 2013). In the  
 316 case of molten material induced by a giant impact, a significant fraction of the atmosphere  
 317 (if any) can be eroded from the impacted body (Shuvalov, 2009) which strongly enhances the  
 318 excess heat removal and decreases the cooling and solidification times. Hence, the duration  
 319 of the partially molten stage decreases from more than 1 million years with an atmosphere  
 320 to  $\sim 1000$  years when no atmosphere is present (Lebrun et al., 2013). The two crust forma-  
 321 tion scenarios give identical dichotomies for non-reversing dynamos (Amit et al., 2011). In  
 322 the reversing case, if the crust was formed over a period much longer than a typical magnetic  
 323 timescale, the continuous scenario is relevant (Dietrich and Wicht, 2013). Conversely, if the  
 324 crust was formed faster than a typical magnetic timescale (i.e. without any atmosphere), the  
 325 random scenario is relevant (see Fig. 3).

### 326 **3 Influence of impact heating on core dynamo**

327 Various CMB heat flux models corresponding to varying impactor sizes were examined. We  
 328 considered two extreme geographic locations of the impactor, with a center falling on the geo-  
 329 graphical pole or on the equator. The impactor introduces warm material to the lower mantle,

330 thus locally decreases the CMB heat flux. Apart from pattern dependence, the reduction in  
331 mean CMB heat flux (expressed by the  $Ra$  number compared to its reference homogeneous  
332 case) as well as the amplitude of the heat flux heterogeneity  $q^*$  are all dependent in a self-  
333 consistent manner on the radius of the impactor. A larger impactor warms a larger part of the  
334 CMB, thus reduces the mean CMB heat flux  $q_0$  more and produces larger  $q^*$  (see Table 1).

335 Fig. 4 shows the time-average rms radial field at the CMB and the time-average field  
336 intensity at the surface of Mars for case I2 with an impactor of radius 800 km falling on  
337 the north geographic pole. Here and elsewhere all magnetic field values are given in units  
338 of  $\sqrt{\rho\mu_0\lambda\Omega}$  where  $\rho$  is the fluid density and  $\mu_0$  is permeability of free space. The impactor  
339 yields an hemispheric field similar to those obtained with synthetic  $Y_1^0$  CMB heat flux patterns  
340 (Stanley et al., 2008; Amit et al., 2011; Dietrich and Wicht, 2013).

341 Fig. 5 shows the time-average zonal temperature and flow in case I2. The reduced CMB  
342 heat flux in the north pole region caused by the impactor results in a relatively warmer fluid  
343 there. The colder fluid in the more vigorously convecting southern hemisphere is associated  
344 with fluid downwelling at high-latitudes that concentrates the magnetic field. This produces a  
345 south-north magnetic hemispheric dichotomy. In addition, the boundary driven thermal wind  
346 flow exhibits a large one cell meridional circulation with surface flow going southward, carry-  
347 ing weak magnetic flux from north to south. These dynamical features are also in agreement  
348 with that obtained with a synthetic  $Y_1^0$  CMB heat flux pattern (Stanley et al., 2008; Amit et al.,  
349 2011).

350 When the impactor is falling on the equatorial plane, some magnetic dichotomy may be  
351 expected between eastern and western hemispheres. Indeed Fig. 6 shows that in case I5  
352 such a dichotomy is obtained. Note that the east-west dichotomy in this case is significantly  
353 weaker than the south-north dichotomy in the corresponding polar impactor case I2 with the  
354 same impactor radius of 800 km. However, compared to the east-west dichotomy obtained  
355 with a synthetic  $Y_1^1$  CMB heat flux pattern (Amit et al., 2011), the impactor driven east-west  
356 dichotomy is significantly stronger (compare cases I5 and Y3 in Table 1).

357 Fig. 7 shows two snapshots of the radial field at the CMB and the intensity at the surface  
358 of Mars for case I3 with the largest impactor studied here (radius of 1000 km) falling on the

359 north geographic pole as well as the corresponding long term time-average surface intensity.  
360 The differences between the two snapshots attest to the chaotic time dependence of this model.  
361 Nevertheless, in both snapshots the relatively small-scale radial field at the CMB is strongest at  
362 high latitudes of the southern hemisphere. The surface intensity is large scale, and also peaks  
363 at the polar region of the southern hemisphere. In this case, the time-average south-north  
364 dichotomy is 2.25 (see Table 1), very close to the lower bound estimation of 2.4 obtained by  
365 Amit et al. (2011) based on observations of the martian crustal magnetic field (Langlais et al.,  
366 2004).

367 Finally we examine the influence of the strength of the internal core convection. Case  
368 I4 is identical to case I3 except for its  $Ra$  value which is larger. The south-north magnetic  
369 dichotomy in this case is 2.58 (Table 1), demonstrating that more vigorous core convection  
370 produces more hemispherical fields.

371 Our models show that a polar impactor leads to a stronger north-south hemispheric mag-  
372 netic dichotomy than an equatorial impactor to an east-west dichotomy. We also find that in  
373 the non-reversing regime of parameters, the magnetic field dichotomy that can be recorded  
374 in the cooling IIMM is independent of the crust formation scenario (random or continuous).  
375 Reversing dynamos that convect stronger produce stronger magnetic dichotomies than non-  
376 reversing dynamos. These results are in agreement with those obtained by Amit et al. (2011)  
377 for degree-1 heat flux patterns.

378 The amplitude of the CMB heat flux heterogeneity (Fig. 2) is commonly measured by the  
379 peak to peak lateral variation (Olson and Christensen, 2002). However, when the pattern is not  
380 smooth and very localized, with imbalance between areas of positive and negative anomalies,  
381  $q^*$  is inadequate. This is exactly the case in the impact driven heat flux patterns considered here.  
382 For example, for very small impacts the amplitude is negligible but  $q^*$  approaches 0.5 (Fig.  
383 1b). We quantify the impact driven heterogeneity amplitude by  $q_0^r$  (Eq. 1) which measures  
384 the extent of the CMB surface affected by the impact heating. Therefore, in order to compare  
385 the efficiency of magnetic hemispheric dichotomy generation by impact driven patterns with  
386 the efficiency by synthetic degree-1 patterns,  $q_0^r$  in the first must be compared with  $q^*$  in the  
387 latter. In addition we propose that the governing parameter controlling the amplitude of the

388 hemispheric magnetic dichotomy is the horizontal Rayleigh number  $Ra_h$  (Willis et al., 2007).  
 389 We define  $Ra_h$  as:

$$Ra_h = \begin{cases} q^* Ra & \text{in Y cases} \\ q_0^r Ra & \text{in I cases} \end{cases} \quad (11)$$

390 To adequately compare the synthetic  $Y_1^0$  CMB heat flux cases from Amit et al. (2011) and  
 391 the polar impact driven CMB heat flux cases from this study, we plot in Fig. 8 the increase  
 392 of the south-north dichotomy  $SN - 1$  as a function of  $Ra_h$  (11). This figure shows that  
 393 for a given lateral forcing, an impact induced CMB heat flux heterogeneity is significantly  
 394 more efficient than a synthetic  $Y_1^0$  CMB heat flux heterogeneity in generating hemispheric  
 395 magnetic dichotomies. It also shows that the impactor size needed to generate the observed  
 396 martian dichotomy (Amit et al., 2011) is slightly larger than 1000 km, which is within the  
 397 estimated range of impactor sizes (Marinova et al., 2008). The better efficiency of impact  
 398 driven hemispheric dynamos over the synthetic cases is even more pronounced in the equatorial  
 399 cases (see Table 1).

## 400 **4 Implication for crustal magnetic dichotomy**

401 Our results show that large  $Ra_h$  (and therefore large  $Ra$ ) are needed in order to get a dichotomy  
 402 as strong as the observed. As large  $Ra$  are likely to be associated with reversing dynamos (e.g.  
 403 Kutzner and Christensen, 2002), the answer depends on the duration of a chron relative to the  
 404 duration of the crystallization of the IIMM induced by the impact. If a slow crystallization rate  
 405 was coupled with short magnetic chrons (Dietrich and Wicht, 2013), then our models cannot  
 406 explain the observed martian dichotomy. However, if a relatively rapid magma cooling was  
 407 coupled with a relatively low reversal frequency then the impact induced magnetic dichotomy  
 408 may have been recorded within the martian crust and explain the observed signal. Hence, the  
 409 relevant magnetic timescale is a duration of a typical chron.

410 In our non-reversing dynamo models the chron duration is effectively infinite and the hemi-  
 411 spheric magnetic dichotomies may be recorded by the crustal magnetization (Fig. 3, left).  
 412 However, the amplitudes of the dichotomies in these cases are too low to explain the observed

413 hemispheric crustal magnetic dichotomy on Mars (Table 1). Dynamo models with large am-  
414 plitude hemispheric dichotomies tend to reverse frequently, in agreement with the findings of  
415 Dietrich and Wicht (2013). For example, in case I3 a typical chron persists for  $\sim 18$  kyr. In  
416 order for such a model to record an hemispheric magnetic dichotomy at the crust, very fast  
417 crust formation is required.

418 Dietrich et al. (2013) studied hemispherical dynamos in the framework of classical mean  
419 field theory. For  $q^* > 0.6$  Dietrich and Wicht (2013) found hemispheric  $\alpha\Omega$  dynamos with  
420 fast oscillations over periods of  $\sim 10$  kyrs. In our models the amplitude of CMB heat flux  
421 heterogeneity is moderate with  $q^* \sim 0.6$ , and more importantly  $q_0^r \ll 0.6$ . Our dynamos are  
422 therefore of the  $\alpha^2$ -type with chaotic (reversing or non-reversing) behaviour. In addition, the  
423 moderate  $q_0^r$  does not change the dynamo regime from stable to reversing. In these dynamos  
424 the duration of a chron (or the reversal frequency) depends on the level of turbulence in the core  
425 (Olson and Amit, 2014), which is in general unknown (even for the Earth). Chron duration  
426 varied immensely over Earth's history between 40 kyrs - 40 Myrs (Merrill et al., 1998).

427 Fig. 9 illustrates the interplay between the relevant time-scales: the crystallization time  $\tau_c$ ,  
428 the spreading time  $\tau_{imp}$  and the duration of a chron. In the context of a martian giant impact,  
429 the associated molten thickness  $\delta$  ranges between 30 and 50 km and the melt fraction is  $\sim$   
430 20 % (Marinova et al., 2008). Hence, the crystallization and cooling times of the shallow  
431 IIMM induced by one impact should be rapid: even if the complete solidification timescale  
432 ultimately depends on the poorly constrained evolution of the post-impact transient atmosphere  
433 (Abe, 1997), crystallization of this local molten material should occur in less than 1000 yr  
434 (Reese and Solomatov, 2006). The subsequent evolution of the partially molten material could  
435 involve isostatic readjustment of a deep, initially hemispheric, retained melt region and lateral  
436 spreading as a gravity current (Reese et al., 2011). Overall, the surface temperature of the  
437 IIMM falls below the Curie temperature in a timescale that strongly depends on factors such  
438 as the characteristics of the above atmosphere or the viscosity of the solid mantle if isostatic  
439 rebound is involved. This instant characterizes the beginning of the time interval when the  
440 solidified crust starts to record the magnetic field. The cold front then propagates downwards  
441 from the surface and a secondary front most probably develops at the base of the IIMM whose  
442 nature depends on the thermal state of the pre-impact crust on top of which the IIMM is

443 superimposed (Fig. 9). The crustal material originating in the impact event stops recording the  
444 magnetic field precisely when the innermost region is cooler than the Curie temperature. In  
445 summary, given these somewhat overlapping ranges of timescales for the crust formation and  
446 magnetic chrons, we argue that both end-member crust formation scenarios are in principle  
447 possible, bearing in mind that reality may be somewhere in between.

448 Our study also emphasizes the importance of the duration of the post-impact thermal  
449 anomaly at the CMB ( $\tau_{imp}$ ). If this timescale is shorter than the time needed by the IIMM  
450 to cool down to temperatures smaller than the Curie temperature  $\tau_c$ , the hemispheric dynamo  
451 has ended before the crust was able to record it. However, if  $\tau_{imp}$  is larger than  $\tau_c$ , the post-  
452 impact magnetic field can be recorded within the crust. The beginning of this record starts at  
453  $\tau_{c,top} \sim 1$  kyr and ends at  $\tau_{c,int} \sim 10 - 100$  Myr, this time interval being mostly controlled by  
454 heat diffusion. The deep post-impact thermal re-adjustment occurs within a characteristic time  
455 that is governed by the rheology of the mantle surrounding the post-impact thermal anomaly.  
456 For a mantle viscosity comparable to that of the present day Earth, say around  $10^{21}$  Pa.s, this  
457 characteristic spreading time is  $\tau_{imp} \sim 10 - 100$  Myr (Monteux et al., 2007; Watters et al.,  
458 2009) which is much larger than the characteristic magnetic diffusion time  $\tau_\lambda \sim 30$  kyrs (e.g.  
459 Bloxham and Jackson, 1991) or the time needed by the top of the IIMM to reach the Curie  
460 temperature  $\tau_{c,top}$  (Fig. 9).

## 461 5 Conclusion

462 Can the observed martian hemispheric magnetic dichotomy be the consequence of a giant  
463 impact that has led to an internal hemispheric magnetic field? Our results show that a  $\sim 1000$   
464 km radius impactor can generate a sufficiently large scale thermal anomaly at the CMB so  
465 that a hemispheric dynamo is generated. An impact induced CMB heat flux heterogeneity  
466 is more efficient than a synthetic degree-1 CMB heat flux heterogeneity in generating strong  
467 hemispheric magnetic dichotomies. This magnetic dichotomy is stronger for a polar impact  
468 than for an equatorial impact. This result reconciles the giant impact induced scenario evoked  
469 to explain the martian topographic dichotomy (Andrews-Hanna et al., 2008; Marinova et al.,  
470 2008; Nimmo et al., 2008) and the heterogeneous CMB heat flux scenario proposed to explain

471 why the magnetization is strong only in the southern hemisphere (Stanley et al., 2008) via  
472 a more realistic CMB heat flux pattern than the previously used synthetic degree-1. Hence,  
473 we propose here that an external event at the martian surface may have produced an internal  
474 hemispheric dynamo.

475 From our results, three relevant timescales arise: the cooling time of the impact induced  
476 molten material, the duration of a magnetic chron and the duration of the post-impact thermal  
477 anomaly at the CMB. The first is mainly governed by the characteristics of the martian atmo-  
478 sphere, the second is governed by the core dynamics while the third is governed by the mantle  
479 dynamics. If a relatively rapid magma cooling was coupled with a relatively low reversal  
480 frequency and with a stable CMB heat flux heterogeneity, then the impact induced magnetic  
481 dichotomy may have been recorded within the martian crust and explain the observed signal.

482 According to some studies (e.g. Arkani-Hamed and Olson, 2010), a giant impact might  
483 have led to a thermal stratification at the top of the core that terminated the dynamo. How-  
484 ever, core stratification can be removed much faster by convection of molten material, over a  
485 timescale orders of magnitude shorter than the longevity of mantle thermal anomalies. Hence  
486 our scenario of giant impact leading to heterogenous mantle heating and to a hemispheric  
487 dynamo on Mars may follow an episode of dynamo shutdown.

488 Our impact driven CMB heat flux heterogeneity model may also be applied to model dy-  
489 namos of other planets. Indeed, giant impacts were common in the later stage of accretion of  
490 terrestrial planets. The Earth is likely formed by accretion of a few dozen moon to Mars-size  
491 planetary embryos (see review by Chambers, 2004). A Mars-size impact on Earth may have  
492 resulted in the formation of the Moon (Hartmann and Davis, 1975; Cameron and Ward, 1976;  
493 Canup, 2004). The Moon was also probably hit by a large planetesimal at the end of its forma-  
494 tion (Jutzi and Asphaug, 2011). Finally, an oblique collision of a large body with a mass about  
495 one sixth of Mercury's has likely stripped away a significant part of its mantle (Smith, 1979;  
496 Benz et al., 1988). Furthermore, these three terrestrial objects have or have had an internally  
497 generated magnetic field (Stevenson, 2003). Hence, giant impacts have potentially strongly  
498 influenced their internal dynamics and dynamo activities.

## 499 **Acknowledgments**

500 J. Monteux was funded by Agence Nationale de la Recherche (Accretis decision no. ANR-  
501 10-PDOC-001-01). We thank Johannes Wicht for providing the MAGIC code. We thank  
502 two anonymous reviewers for their careful and insightful reviews that greatly improve the  
503 manuscript. The authors also thank N. Mangold and J.P. Lorand for useful discussions.

## References

- 504 **References**
- 505 Abe, Y., 1997. Thermal and chemical evolution of the terrestrial magma ocean. *Phys. Earth*  
506 *Planet. Inter.* 100, 27–39.
- 507 Acuña, M., Connerney, J., Wasilewski, P., Lin, R., Anderson, K., Carlson, C., McFadden, J.,  
508 Curtis, D., Mitchell, D., Reme, H., Mazelle, C., Sauvaud, J., d’Uston, C., Cros, A., Medale,  
509 J., Bauer, S., Cloutier, P., Mayhew, M., Winterhalter, D., Ness, N., 1998. Magnetic field and  
510 plasma observations at Mars: Initial results of the Mars global surveyor mission. *Science*  
511 279 (5357), 1676–1680.
- 512 Amit, H., Aubert, J., Hulot, G., 2010. Stationary, oscillating or drifting mantle-driven geomag-  
513 netic flux patches? *J. Geophys. Res.* 115, B07108.
- 514 Amit, H., Choblet, G., 2009. Mantle-driven geodynamo features - effects of post-Perovskite  
515 phase transition. *Earth, Planets, and Space* 61, 1255–1268.
- 516 Amit, H., Choblet, G., 2012. Mantle-driven geodynamo features - Effects of compositional  
517 and narrow D” anomalies. *Phys. Earth Planet. Inter.* 190, 34–43.
- 518 Amit, H., Christensen, U., Langlais, B., 2011. The influence of degree-1 mantle heterogeneity  
519 on the past dynamo of Mars. *Phys. Earth Planet. Inter.* 189, 63–79.
- 520 Anderson, B. J., Johnson, C. L., Korth, H., Winslow, R. M., Borovsky, J. E., Purucker, M. E.,  
521 Slavin, J. A., Solomon, S. C., Zuber, M. T., McNutt, Jr., R. L., Dec. 2012. Low-degree  
522 structure in Mercury’s planetary magnetic field. *J. Geophys. Res. (Planets)* 117, 0.
- 523 Andrews-Hanna, J. C., Zuber, M. T., Banerdt, W. B., 2008. The Borealis basin and the origin  
524 of the martian crustal dichotomy. *Nature* 453, 1212–1215.
- 525 Arkani-Hamed, J., Olson, P., 2010. Giant impact stratification of the Martian core. *Geophys.*  
526 *Res. Lett.* 37, L02201.
- 527 Asphaug, E., Agnor, C. B., Williams, Q., 2006. Hit-and-run planetary collisions. *Nature* 439,  
528 155–160.

- 529 Aubert, J., Amit, H., Hulot, G., 2007. Detecting thermal boundary control in surface flows  
530 from numerical dynamos. *Phys. Earth Planet. Inter.* 160, 143–156.
- 531 Aubert, J., Amit, H., Hulot, G., Olson, P., 2008. Thermo-chemical wind flows couple Earth's  
532 inner core growth to mantle heterogeneity. *Nature* 454, 758–761.
- 533 Aubert, J., Labrosse, S., Poitou, C., 2009. Modelling the paleo-evolution of the geodynamo.  
534 *Geophys. J. Int.* 179, 1414–1428.
- 535 Benz, W., Slattery, W. L., Cameron, A. G. W., 1988. Collisional stripping of Mercury's mantle.  
536 *Icarus* 74, 516–528.
- 537 Bloxham, J., 2002. Time-independent and time-dependent behaviour of high-latitude flux bun-  
538 dles at the core-mantle boundary. *Geophys. Res. Lett.* 29, 1854.
- 539 Bloxham, J., Jackson, A., 1991. Fluid flow near the surface of the Earth's outer core. *Rev.*  
540 *Geophys.* 29, 97–120.
- 541 Breuer, D., Labrosse, S., Spohn, T., 2010. Thermal Evolution and Magnetic Field Generation  
542 in Terrestrial Planets and Satellites. *Space Sci. Rev.* 152, 449–500.
- 543 Cameron, A. G. W., Ward, W. R., 1976. The Origin of the Moon. In: *Lun. Planet. Inst. Conf.*  
544 *Abs. Vol. 7.* pp. 120–122.
- 545 Canup, R. M., 2004. Simulations of a late lunar-forming impact. *Icarus* 168, 433–456.
- 546 Cao, H., Aurnou, J. M., Wicht, J., Dietrich, W., Soderlund, K. M., Russell, C. T., 2014. A  
547 dynamo explanation for Mercury's anomalous magnetic field. *Geophys. Res. Lett.* 41, 4127–  
548 4134.
- 549 Chambers, J. E., 2004. Planetary accretion in the inner Solar System. *Earth Planet. Sci. Lett.*  
550 223, 241–252.
- 551 Chassefière, E., Langlais, B., Quesnel, Y., Leblanc, F., 2013. The fate of early Mars' lost water:  
552 The role of serpentinization. *J. Geophys. Res. (Planets)* 118, 1123–1134.

- 553 Dietrich, W., Schmitt, D., Wicht, J., 2013. Hemispherical Parker waves driven by thermal shear  
554 in planetary dynamos. *Europhys. Lett.* 104.
- 555 Dietrich, W., Wicht, J., 2013. A hemispherical dynamo model: Implications for the Martian  
556 crustal magnetization. *Phys. Earth Planet. Int.* 217, 10–21.
- 557 Elkins-Tanton, L. T., Parmentier, E. M., Hess, P. C., 2003. Magma ocean fractional crystal-  
558 lization and cumulate overturn in terrestrial planets: Implications for Mars. *Meteoritics and*  
559 *Planetary Science* 38, 1753–1771.
- 560 Elkins-Tanton, L. T., Zaranek, S. E., Parmentier, E. M., Hess, P. C., 2005. Early magnetic field  
561 and magmatic activity on Mars from magma ocean cumulate overturn. *Earth and Planetary*  
562 *Science Letters* 236, 1–12.
- 563 Frey, H. V., Roark, J. H., Shockey, K. M., Frey, E. L., Sakimoto, S. E. H., 2002. Ancient  
564 lowlands on Mars. *Geophys. Res. Lett.* 29, 1384.
- 565 Gladman, B., Coffey, J., 2009. Mercurian impact ejecta: Meteorites and mantle. *Meteoritics*  
566 *Planet. Sci.* 44, 285–291.
- 567 Glatzmaier, G., Coe, R., Hongre, L., Roberts, P., 1999. The role of the earth's mantle in con-  
568 trolling the frequency of geomagnetic reversals. *Nature* 401, 885–890.
- 569 Golabek, G. J., Gerya, T. V., Kaus, B. J. P., Ziethe, R., Tackley, P. J., 2009. Rheological controls  
570 on the terrestrial core formation mechanism. *Geochemistry, Geophysics, Geosystems* 10,  
571 Q11007.
- 572 Gubbins, D., Willis, P. W., Sreenivasan, B., 2007. Correlation of Earth's magnetic field with  
573 lower mantle thermal and seismic structure. *Phys. Earth Planet. Inter.* 162, 256–260.
- 574 Harder, H., Christensen, U., 1996. A one-plume model of Martian mantle convection. *Nature*  
575 380, 507–509.
- 576 Hartmann, W. K., Davis, D. R., 1975. Satellite-sized planetesimals and lunar origin. *Icarus* 24,  
577 504–514.

- 578 Hori, K., Wicht, J., Christensen, U., 2010. The effect of thermal boundary conditions on dy-  
579 namos driven by internal heating. *Phys. Earth Planet. Inter.* 182, 85–97.
- 580 Hori, K., Wicht, J., Dietrich, W., 2014. Ancient dynamos of terrestrial planets more sensitive  
581 to core-mantle boundary heat flows. *Planet. Space. Sci.* 98, 30–40.
- 582 Jutzi, M., Asphaug, E., 2011. Forming the lunar farside highlands by accretion of a companion  
583 moon. *Nature* 476, 69–72.
- 584 Ke, Y., Solomatov, V. S., 2006. Early transient superplumes and the origin of the Martian  
585 crustal dichotomy. *Journal of Geophysical Research (Planets)* 111, 10001.
- 586 Kutzner, C., Christensen, U., 2002. From stable dipolar towards reversing numerical dynamos.  
587 *Phys. Earth Planet. Inter.* 131, 29–45.
- 588 Kutzner, C., Christensen, U. R., 2004. Simulated geomagnetic reversals and preferred virtual  
589 geomagnetic pole paths. *Geophys. J. Int.* 157, 1105–1118.
- 590 Langlais, B., Amit, H., 2008. The past martian dynamo. *Science* 321, 1784–1785.
- 591 Langlais, B., Purucker, M., Manda, M., 2004. Crustal magnetic field of Mars. *J. Geophys.*  
592 *Res.* 109, E02008.
- 593 Langlais, B., Thébault, E., 2011. Predicted and observed magnetic signatures of martian  
594 (de)magnetized impact craters. *Icarus* 212, 568–578.
- 595 Le Feuvre, M., Wieczorek, M. A., 2011. Nonuniform cratering of the Moon and a revised  
596 crater chronology of the inner Solar System. *Icarus* 214, 1–20.
- 597 Lebrun, T., Massol, H., Chassefière, E., Davaille, A., Marcq, E., Sarda, P., Leblanc, F., Bran-  
598 deis, G., Jun. 2013. Thermal evolution of an early magma ocean in interaction with the  
599 atmosphere. *Journal of Geophysical Research (Planets)* 118, 1155–1176.
- 600 Lillis, R. J., Frey, H. V., Manga, M., 2008. Rapid decrease in Martian crustal magnetization  
601 in the Noachian era: Implications for the dynamo and climate of early Mars. *Geophys. Res.*  
602 *Lett.* 35, 14203.

- 603 Lillis, R. J., Stewart, S. T., Manga, M., 2013. Demagnetization by basin-forming impacts on  
604 early Mars: Contributions from shock, heat, and excavation. *J. Geophys. Res. (Planets)* 118,  
605 1045–1062.
- 606 Marinova, M. M., Aharonson, O., Asphaug, E., 2008. Mega-impact formation of the Mars  
607 hemispheric dichotomy. *Nature* 453, 1216–1219.
- 608 Marinova, M. M., Aharonson, O., Asphaug, E., 2011. Geophysical consequences of planetary-  
609 scale impacts into a Mars-like planet. *Icarus* 211, 960–985.
- 610 Merrill, R., McElhinny, M., McFadden, P., 1998. *The Magnetic Field of the Earth: Paleomag-*  
611 *netism, the Core, and the Deep Mantle*. Academic Press, San Diego, California, USA.
- 612 Monteux, J., Arkani-Hamed, J., 2014. Consequences of giant impacts in early Mars: Core  
613 merging and Martian dynamo evolution. *J. Geophys. Res. (Planets)* 119, 480–505.
- 614 Monteux, J., Coltice, N., Dubuffet, F., Ricard, Y., 2007. Thermo-mechanical adjustment after  
615 impacts during planetary growth. *Geophys. Res. Lett.* 34, 24201–24205.
- 616 Monteux, J., Jellinek, A. M., Johnson, C. L., 2011. Why might planets and moons have early  
617 dynamos? *Earth Planet. Sci. Lett.* 310, 349–359.
- 618 Monteux, J., Jellinek, A. M., Johnson, C. L., 2013. Dynamics of core merging after a mega-  
619 impact with applications to Mars’ early dynamo. *Icarus* 226, 20–32.
- 620 Nimmo, F., Hart, S. D., Korycansky, D. G., Agnor, C. B., 2008. Implications of an impact  
621 origin for the martian hemispheric dichotomy. *Nature* 453, 1220–1223.
- 622 Olson, P., 2007. Gravitational dynamos and the low frequency geomagnetic secular variation.  
623 *Proc. Nat. Acad. Sci.* 104, 20159–20166.
- 624 Olson, P., Amit, H., 2014. Magnetic reversal frequency scaling in dynamos with thermochem-  
625 ical convection. *Phys. Earth Planet. Inter.* 229, 122–133.
- 626 Olson, P., Christensen, U., 2002. The time averaged magnetic field in numerical dynamos with  
627 nonuniform boundary heat flow. *Geophys. J. Int.* 151, 809–823.

- 628 Olson, P., Coe, R. S., Driscoll, P. E., Glatzmaier, G. A., Roberts, P. H., 2010. Geodynamo  
629 reversal frequency and heterogeneous core-mantle boundary heat flow. *Phys. Earth Planet.*  
630 *Inter.* 180, 66–79.
- 631 Olson, P., Deguen, R., Hinnov, L. A., Zhong, S., 2013. Controls on geomagnetic reversals  
632 and core evolution by mantle convection in the Phanerozoic. *Phys. Earth Planet. Inter.* 214,  
633 87–103.
- 634 Parker, R., 2003. Ideal bodies for Mars magnetism. *JOURNAL OF GEOPHYSICAL*  
635 *RESEARCH-PLANETS* 108 (E1).
- 636 Pierazzo, E., Melosh, H. J., 2000. Melt Production in Oblique Impacts. *Icarus* 145, 252–261.
- 637 Pierazzo, E., Vickery, A. M., Melosh, H. J., 1997. A Reevaluation of Impact Melt Production.  
638 *Icarus* 127, 408–423.
- 639 Pozzo, M., Davies, C., Gubbins, D., Alfè, D., 2012. Thermal and electrical conductivity of  
640 iron at Earth's core conditions. *Nature* 485, 355–358.
- 641 Quesnel, Y., Sotin, C., Langlais, B., Costin, S., Manda, M., Gottschalk, M., Dymont, J., 2009.  
642 Serpentinization of the martian crust during Noachian. *Earth Planet. Sci. Lett.* 277, 184–193.
- 643 Reese, C. C., Orth, C. P., Solomatov, V. S., 2010. Impact origin for the Martian crustal di-  
644 chotomy: Half emptied or half filled? *J. Geophys. Res. (Planets)* 115 (14), 5004–+.
- 645 Reese, C. C., Orth, C. P., Solomatov, V. S., 2011. Impact megadomes and the origin of the  
646 martian crustal dichotomy. *Icarus* 213, 433–442.
- 647 Reese, C. C., Solomatov, V. S., 2006. Fluid dynamics of local martian magma oceans. *Icarus*  
648 184, 102–120.
- 649 Reese, C. C., Solomatov, V. S., 2010. Early martian dynamo generation due to giant impacts.  
650 *Icarus* 207, 82–97.
- 651 Roberts, J., Zhong, S., 2006. Degree-1 convection in the Martian mantle and the origin of the  
652 hemispheric dichotomy. *J. Geophys. Res.* 111, E06013.

- 653 Roberts, J. H., Arkani-Hamed, J., 2012. Impact-induced mantle dynamics on Mars. *Icarus* 218,  
654 278–289.
- 655 Roberts, J. H., Lillis, R. J., Manga, M., 2009. Giant impacts on early Mars and the cessation  
656 of the Martian dynamo. *J. Geophys. Res. (Planets)* 114 (13), E04009.
- 657 Rochette, P., 2006. Crustal magnetization of Mars controlled by lithology or cooling rate in a  
658 reversing dynamo? *Geophys. Res. Lett.* 33, 2202.
- 659 Schubert, G., Spohn, T., 1990. Thermal history of Mars and the sulfur content of its core. *J.*  
660 *Geophys. Res.* 95, 14095–14104.
- 661 Senshu, H., Kuramoto, K., Matsui, T., 2002. Thermal evolution of a growing Mars. *J. Geophys.*  
662 *Res.* 107, 1–13.
- 663 Shuvalov, V., Oct. 2009. Atmospheric erosion induced by oblique impacts. *Meteoritics and*  
664 *Planetary Science* 44, 1095–1105.
- 665 Smith, J. V., 1979. *Mineralogy of the Planets: a Voyage in Space and Time.* *Mineralogical*  
666 *Magazine* 43, 1–89.
- 667 Solomon, S. C., Aharonson, O., Aurnou, J. M., Banerdt, W. B., Carr, M. H., Dombard, A. J.,  
668 Frey, H. V., Golombek, M. P., Hauck, S. A., Head, J. W., Jakosky, B. M., Johnson, C. L.,  
669 McGovern, P. J., Neumann, G. A., Phillips, R. J., Smith, D. E., Zuber, M. T., 2005. New  
670 Perspectives on Ancient Mars. *Science* 307, 1214–1220.
- 671 Stanley, S., 2010. A dynamo model for axisymmetrizing Saturn’s magnetic field. *Geophys.*  
672 *Res. Lett.* 37, 5201.
- 673 Stanley, S., Elkins-Tanton, L., Zuber, M. T., Parmentier, E. M., 2008. Mars’ Paleomagnetic  
674 Field as the Result of a Single-Hemisphere Dynamo. *Science* 321, 1822–1825.
- 675 Stevenson, D. J., 2003. Planetary magnetic fields. *Earth Planet. Sci. Lett.* 208, 1–2.
- 676 Tonks, W. B., Melosh, H. J., 1992. Core formation by giant impacts. *Icarus* 100, 326–346.

- 677 Šrámek, O., Ricard, Y., Dubuffet, F., 2010. A multiphase model of core formation. *Geophys.*  
678 *J. Int.* 181, 198–220.
- 679 Watters, W. A., Zuber, M. T., Hager, B. H., 2009. Thermal perturbations caused by large  
680 impacts and consequences for mantle convection. *J. Geophys. Res. (Planets)* 114, E02001.
- 681 Wicht, J., 2002. Inner-core conductivity in numerical dynamo simulations. *Phys. Earth Planet.*  
682 *Inter.* 132, 281–302.
- 683 Wicht, J., Stellmach, S., Harder, H., 2009. Numerical models of the geodynamo: From funda-  
684 mental Cartesian models to 3D simulations of field reversals. In: Glassmeier, H., Soffel, H.,  
685 Nэгendank, J. (Eds.), *Geomagnetic Field Variations - Space-time structure, processes, and*  
686 *effects on system Earth*. Springer, Berlin, pp. 107–158.
- 687 Willis, A. P., Sreenivasan, B., Gubbins, D., 2007. Thermal core mantle interaction: Exploring  
688 regimes for "locked" dynamo action. *Phys. Earth Planet. Inter.* 165, 83–92.
- 689 Yoder, C. F., Konopliv, A. S., Yuan, D. N., Standish, E. M., Folkner, W. M., 2003. Fluid Core  
690 Size of Mars from Detection of the Solar Tide. *Science* 300, 299–303.
- 691 Zhong, S., Zuber, M. T., 2001. Degree-1 mantle convection and the crustal dichotomy on Mars.  
692 *Earth and Planetary Science Letters* 189, 75–84.
- 693 Zuber, M. T., 2001. The crust and mantle of Mars. *Nature* 412, 220–227.

| Case | Pattern    | $R_{imp}$ [km] | $Ra$              | $q^*$ | $q_0^r$ | $Rm$ | $SN_{cnt}$ | $SN_{rnd}$ | $EW_{cnt}$ | $EW_{rnd}$ | $\tau_{ch}$ |
|------|------------|----------------|-------------------|-------|---------|------|------------|------------|------------|------------|-------------|
| I1   | Polar      | 600            | $2.90 \cdot 10^7$ | 0.51  | 0.04    | 386  | -          | 1.18       | -          | -          | 40.9        |
| I2   | Polar      | 800            | $2.69 \cdot 10^7$ | 0.56  | 0.13    | 423  | -          | 1.54       | -          | -          | 22.6        |
| I3   | Polar      | 1000           | $2.21 \cdot 10^7$ | 0.66  | 0.26    | 439  | -          | 2.25       | -          | -          | 18.3        |
| Y1   | $Y_1^0$    | -              | $3 \cdot 10^7$    | 0.8   | -       | 488  | -          | 2.54       | -          | -          | 12.2        |
| I4   | Polar      | 1000           | $4 \cdot 10^7$    | 0.66  | 0.26    | 572  | -          | 2.58       | -          | -          | 15.4        |
| Y2   | $Y_1^1$    | -              | $2 \cdot 10^7$    | 0.8   | -       | 412  | -          | 2.35       | -          | -          | 14.9        |
| I5   | Equatorial | 800            | $2.69 \cdot 10^7$ | 0.56  | 0.13    | 350  | -          | -          | -          | 1.22       | 28.2        |
| Y3   | $Y_1^1$    | -              | $3 \cdot 10^7$    | 0.8   | -       | 405  | -          | -          | -          | 1.14       | 17.5        |
| I6   | Polar      | 800            | $8.97 \cdot 10^6$ | 0.56  | 0.13    | 99   | 1.12       | 1.13       | -          | -          | $\infty$    |
| I7   | Polar      | 1000           | $7.35 \cdot 10^6$ | 0.66  | 0.26    | 182  | 1.59       | 1.57       | -          | -          | $\infty$    |
| Y4   | $Y_1^0$    | -              | $1 \cdot 10^7$    | 0.3   | -       | 114  | 1.16       | 1.16       | -          | -          | $\infty$    |
| Y5   | $Y_1^0$    | -              | $1 \cdot 10^7$    | 0.5   | -       | 157  | 1.49       | 1.50       | -          | -          | $\infty$    |
| I8   | Equatorial | 800            | $8.97 \cdot 10^6$ | 0.56  | 0.13    | 104  | -          | -          | 1.01       | 1.01       | $\infty$    |
| Y6   | $Y_1^1$    | -              | $1 \cdot 10^7$    | 0.5   | -       | 133  | -          | -          | 1.01       | 1.01       | $\infty$    |

Table 1: Summary of numerical dynamo models parameters and resulted magnetic hemispheric dichotomies. In all cases  $r_i/r_o = 0.2$ ,  $Pr = 1$  and  $Pm = 3$ . The upper part includes reversing dynamos with  $E = 3 \cdot 10^{-4}$ ; The lower part includes non-reversing dynamos with  $E = 1 \cdot 10^{-4}$ . The imposed CMB heat flux patterns are either degree-1 single harmonics ( $Y_1^0$  or  $Y_1^1$ ) denoted as cases Y, or impact driven centered at the pole or at the equator denoted as cases I. All Y cases are from Amit et al. (2011) except case Y2 which is from this study. The radius of the impactor is  $R_{imp}$ . The conventional definition of the amplitude of the heat flux anomaly  $q^*$  is defined as the ratio of the peak-to-peak difference to twice the mean (Olson and Christensen, 2002). The reduction in the mean heat flux due to the impact is  $q_0^r$ .  $Rm$  is the magnetic Reynolds number based on the rms velocity in the volume of the shell.  $SN$  and  $EW$  denote *south-north* and *east-west*, 'cnt' and 'rnd' subscripts denote *continuous* and *random* crust formation. East-west ratios are calculated with respect to the hemisphere centered at longitude  $0^\circ$  (center of large heat flux anomaly for  $Y_1^1$  and equatorial I cases) to the hemisphere centered at longitude  $180^\circ$ . For reversing cases only ratios based on random crust formation are given, for  $Y_1^0$  or polar I cases only south-north ratios are given, for  $Y_1^1$  or equatorial I cases only east-west ratios are given. As reference cases, the homogeneous CMB heat flux models from Amit et al. (2011) give  $SN$  and  $EW$  values of unity. The average chron duration  $\tau_{ch}$  is given in kyrs for the reversing cases.

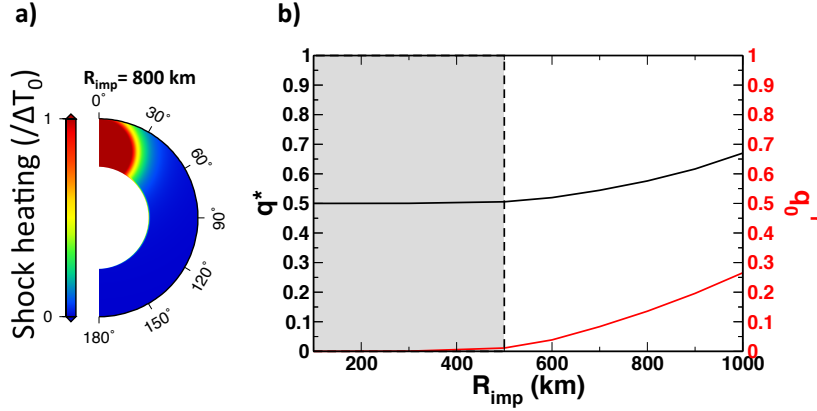


Figure 1: a) martian mantle post-impact temperature increase for  $R_{imp} = 800$  km. b) Corresponding conventional amplitude of heat flux heterogeneity on the CMB  $q^*$  (black line, Eq. 2) and the mean heat flux reduction  $q_0^r$  (red line, Eq. 1) vs. impactor size  $R_{imp}$ . In the grey domain ( $R_{imp} < 500$  km), the impactor is too small for isobaric core to reach the CMB.

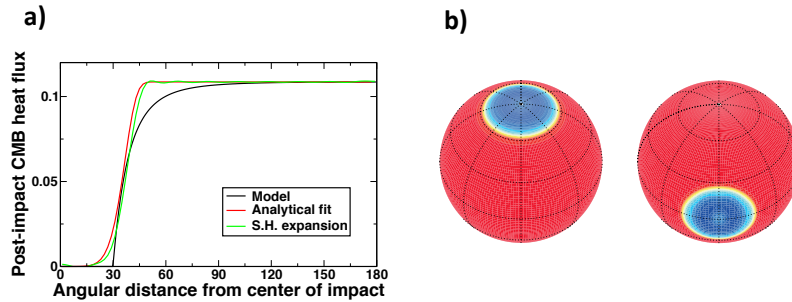


Figure 2: a) Post-impact CMB heat flux (black line), analytical fit (red line) and spherical harmonic expansion (green line) vs. angular distance from the center of the impact driven heated area. b) Imposed CMB heat flux anomalies resulting from an impactor of radius 800 km falling on the north pole (left) or the equator (right).

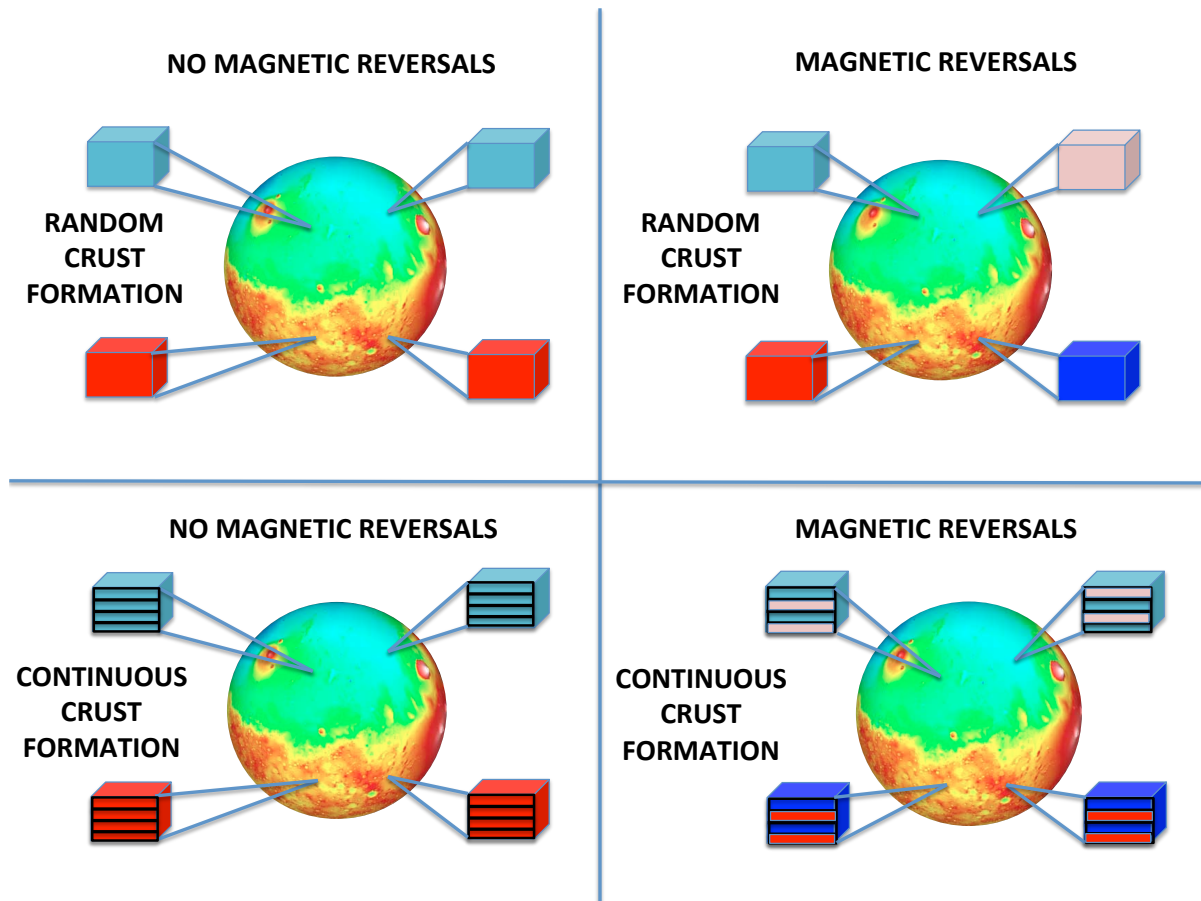


Figure 3: Schematic illustration of the random (top) and continuous (bottom) crust formation scenarios and the corresponding recorded magnetization without (left) or with (right) magnetic reversals. Blue/red denotes negative/positive radial magnetic paleofields respectively, so alternating colors correspond to paleomagnetic reversals. Cubes represent a vertical cut through the martian crust that has recorded strong (deep blue or deep red) or weak (light red or light blue) magnetic paleofields. The weak magnetic paleofield is restricted to the impacted pole while the strong magnetic paleofield is restricted to the opposite one. The current magnetic field observed at the surface results from the vertically integrated magnetization over the cube.

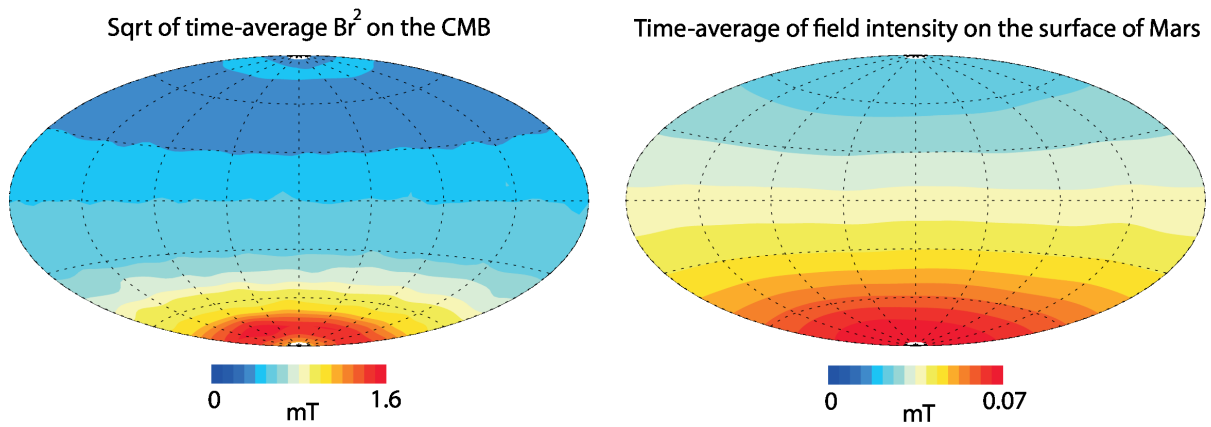


Figure 4: Time-average magnetic field properties on the CMB (left) and on the surface of Mars (right) in case I2. The CMB field is upward continued to the surface of Mars as a potential field.

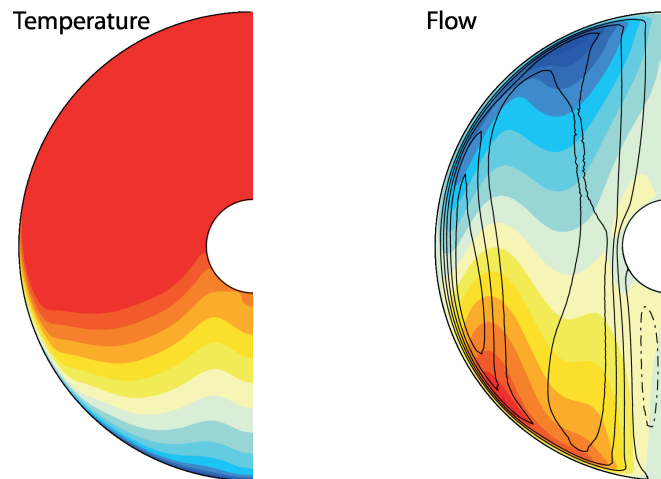


Figure 5: Time-average zonal temperature (left) and flow (right) in case I2. In the right subplot colors denote azimuthal flow and streamlines denote meridional circulation (solid/dashed are anti-clockwise/clockwise respectively).

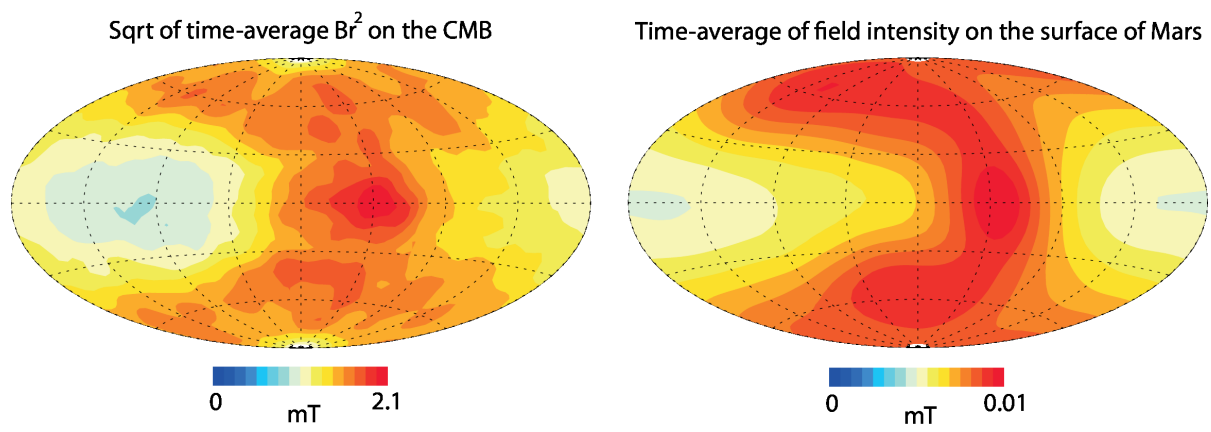


Figure 6: As in Fig. 4 for case I5 (note different color scales).

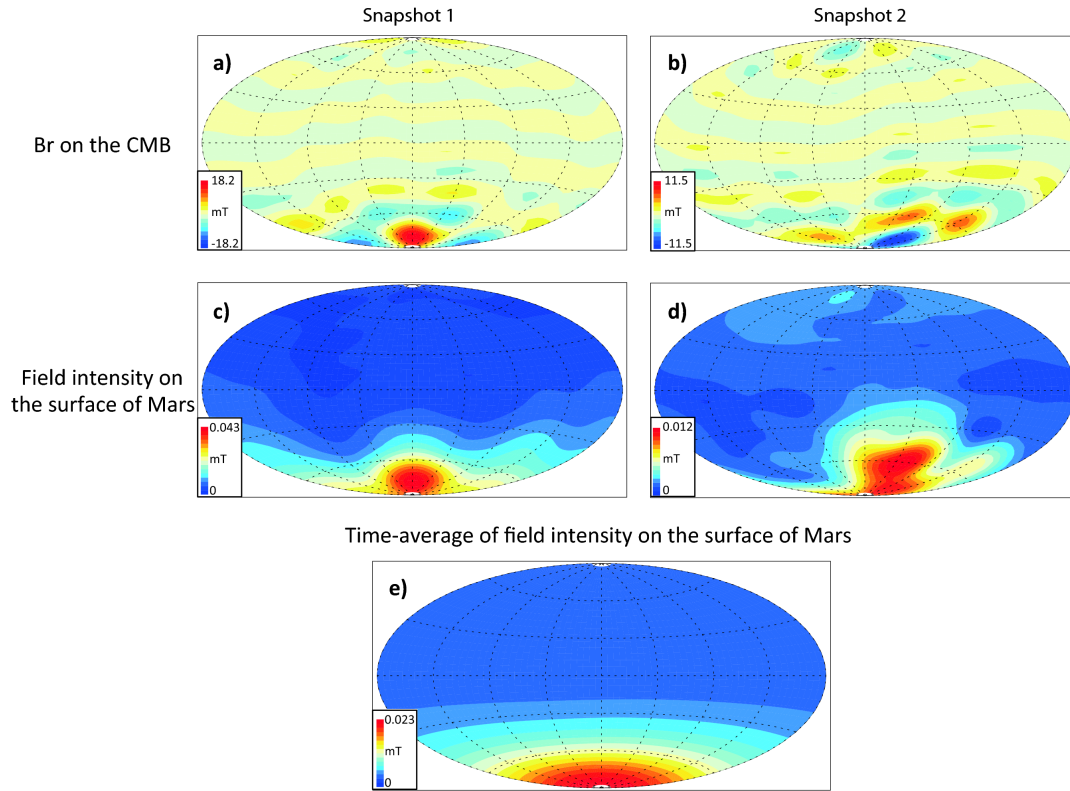


Figure 7: Two arbitrary snapshots (two first lines) of the radial magnetic field  $B_r$  on the core-mantle boundary CMB (a and b) and surface intensity of the magnetic field (c and d) in case I3. The time-average surface intensity is shown on the third line (e). Here the spherical harmonic expansion is truncated at  $\ell_{max} = 10$ . Note differences in color scales among the maps. The CMB field is upward continued to the surface of Mars as a potential field.

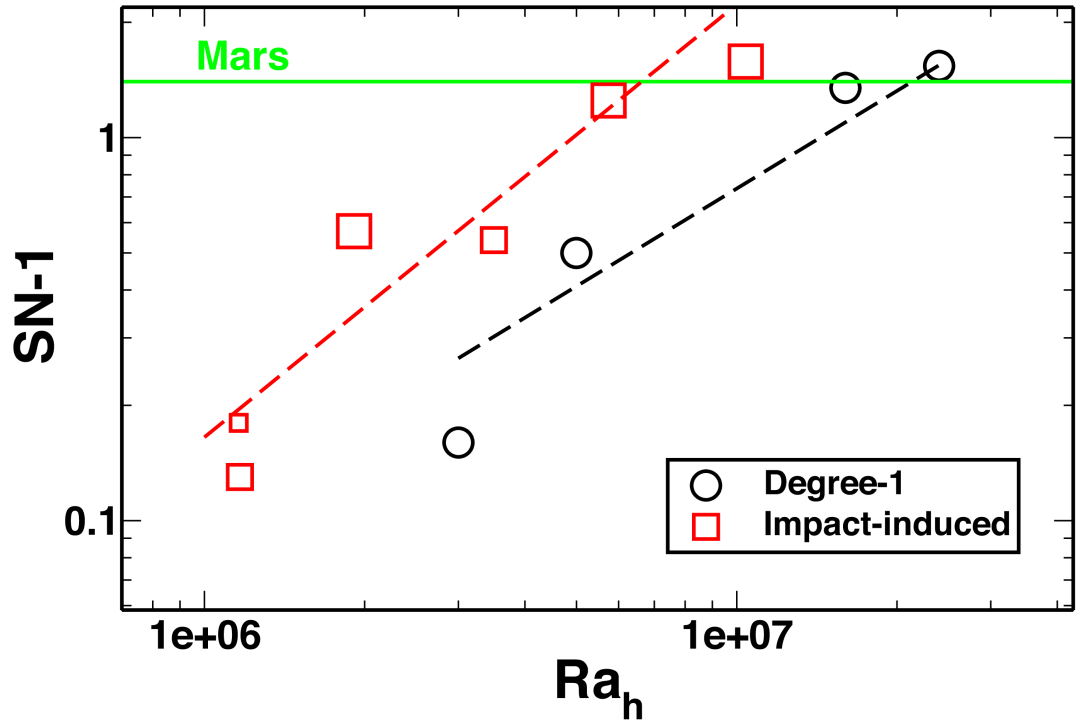


Figure 8: South-north dichotomy as a function of the horizontal Rayleigh number  $Ra_h$  (Eq. 11). The black symbols are the values obtained (with  $r_i/r_o = 0.2$ ) for the synthetic  $Y_1^0$  CMB heat flux patterns (with  $Ra_h = q^* Ra$ ). The red symbols are the values obtained here in cases of polar impact driven CMB heat flux patterns (with  $Ra_h = q_0^r Ra$ ). The size of the red symbols increases with the size of the impactor. The corresponding power law fits are plotted with dashed lines. The green horizontal line represents the martian value of  $SN - 1$  from Amit et al. (2011) based on observations of the martian crustal magnetic field (Langlais et al., 2004). All degree-1 cases are from Amit et al. (2011) except case Y2 from this study (see also Tab. 1).

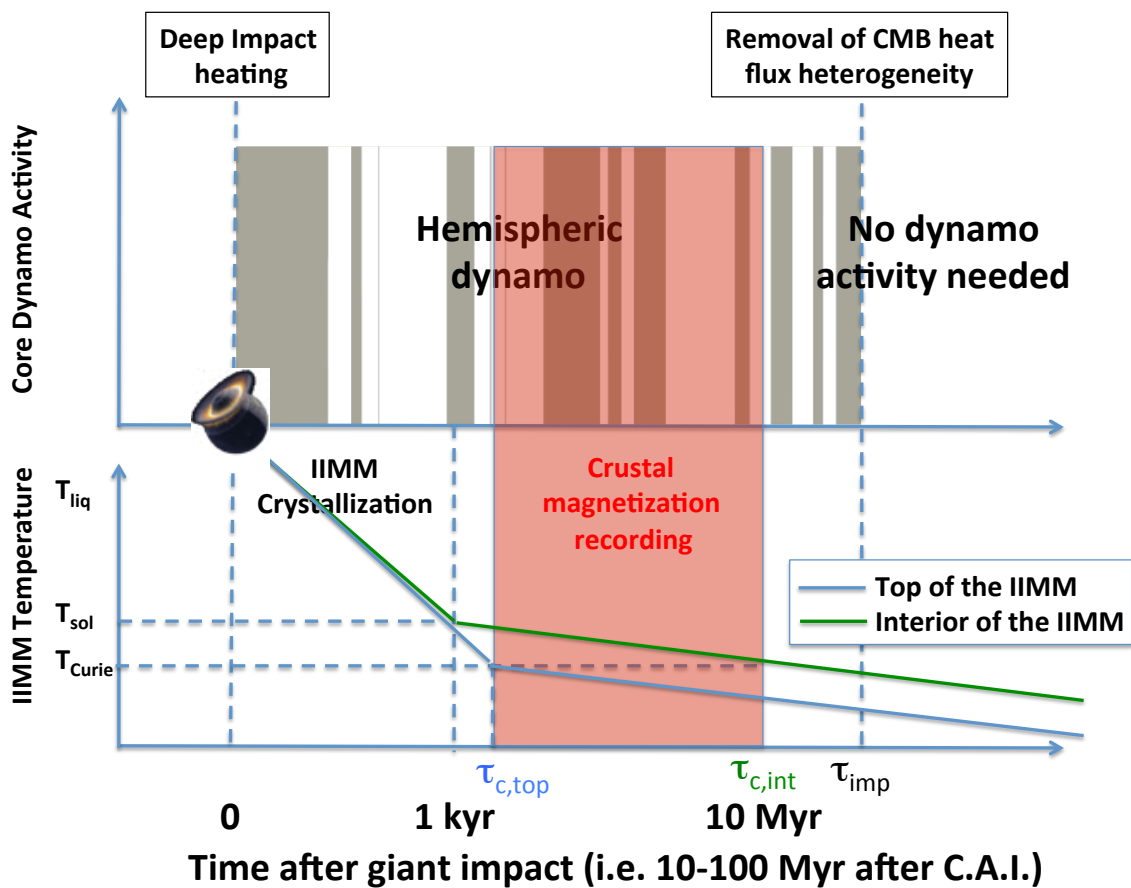


Figure 9: Schematic illustration of temporal evolution of core dynamo activity (top panel) and of the IIMM temperature (bottom panel) after a giant impact. The C.A.I. (Calcium-Aluminium rich Inclusions) are the oldest objects in the solar system. In the bottom panel, the blue line represents the temperature evolution at the interior of the IIMM while the green line represents the top of the IIMM (i.e. the post impact martian surface).